Frontiers of Optoelectronics (2026) 19:24
https://doi.org/10.2738/foe.2026.0024

Frontiers of Optoelectronics

RESEARCH ARTICLE

Chlorinated conjugated copolymer interface modification enables record-efficiency of all-PbS quantum dot tandem solar cells

Salman Ali[1] · Xinzhao Zhao[2] · Mingyu Li[1] · Ruiheng Gao[2] · Tianjun Ma[1] · Yuheng Li[1] · Gomaa Mohamed Gomaa Khalaf[3,6] · Michael Wang[4] · Chris Cheng[4] · Jianbing Zhang[5] · Ahmed Ghitas[6] · Haisheng Song (✉)[1,2,7,8,9] · Jiang Tang[1,2,7,8]

Received: 17 March 2026 / Accepted: 9 May 2026

Abstract
All-lead sulfide (PbS) quantum dot (QD) tandem solar cells (TSCs) offer a promising pathway to surpass single-junction efficiency limits. However, their performance is hindered by the vulnerability of the wide-bandgap (WBG) top cell, which suffers chemical and physical damage during the deposition of 1,2-ethanedithiol (EDT)-capped hole-transport layers (HTLs) and interconnecting layers. This results in morphological voids and interfacial trap states. Here, we introduce a chlorinated benzodithiophene-based conjugated copolymer (D18-Cl) as a multifunctional interfacial passivator at the WBG/HTL interface. D18-Cl could bind to unsaturated Pb sites via chlorine and passivate sulfur vacancies through thiophene ring coordination. This strategy eliminates pinholes and shields the WBG absorber from subsequent processing damage. Furthermore, D18-Cl modification aligns the energy levels by elevating the highest occupied molecular orbital (HOMO) level of the absorber, creating a graded pathway that reduces the hole-extraction barrier and suppresses non-radiative recombination. Consequently, the D18-Cl-modified semitransparent WBG cell achieves a power conversion efficiency (PCE) of 10.36%. When integrated into a monolithic TSC, the device yields a record PCE of 13.148% with an unprecedented fill factor of 73.14%. The encapsulated TSC retains over 90% of its initial PCE after 500 h of MPP tracking, demonstrating exceptional stability.

Keywords Wide-bandgap solar cells · Processing damage · Band alignment · Interface passivation · PbS quantum dots

✉ Haisheng Song
songhs-wnlo@mail.hust.edu.cn

[1] Wuhan National Laboratory for Optoelectronics (WNLO), Huazhong University of Science and Technology (HUST), Wuhan 430074, China
[2] School of Optical and Electronic Information (SOEI), Huazhong University of Science and Technology (HUST), Wuhan 430074, China
[3] College of Engineering Physics, Center for Intense Laser Application Technology, Shenzhen Technology University, Shenzhen 518118, China
[4] Houston Technology Research Center, CNPC USA Corporation (CNPCUSA), Houston 77042, TX, USA
[5] School of Integrated Circuits, Huazhong University of Science and Technology, Wuhan 430074, China
[6] Solar & Space Research Department, National Research Institute of Astronomy and Geophysics (NRIAG), Helwan 11421, Cairo, Egypt
[7] Optics Valley Laboratory (OVL), Wuhan 430074, China
[8] Wenzhou Advanced Manufacturing Technology Research Institute of Huazhong University of Science and Technology, Wenzhou 325035, China
[9] Shenzhen R & D Center, Huazhong University of Science and Technology, Shenzhen 518000, China

1 Introduction

The power conversion efficiency (PCE) of single-junction solar cells (SJSCs) is fundamentally limited by thermalization losses and narrow spectral absorption, which restrict overall device performance [1–3]. Tandem solar cells (TSCs) offer a promising approach to overcoming these limitations by stacking semiconductors with complementary band gaps, thereby enabling broader light absorption, reduced thermalization losses, and an increase in the Shockley–Queisser (SQ) limit from 33% to 45% [4]. Due to their simplified monolithic integration and reduced parasitic absorption compared to 4T configurations, 2T TSCs are preferred tandem architectures, typically comprising a wide-bandgap (WBG) front-illuminated top cell and a narrow-bandgap (NBG) rear bottom cell connected via a recombination layer (RL), and are overwhelmingly favored by the photovoltaic industry [5–8].

Lead sulfide (PbS) colloidal quantum dots (QDs) have been demonstrated as an exceptional candidate for ad-

vanced TSCs. Characterized by a large exciton Bohr radius, PbS QDs offer fine optical bandgap tunability from the visible to the near-infrared, alongside the advantages of solution- and low-temperature processing [9–13]. In highly optimized 2T all-PbS QDs TSC architectures, a 1.40 eV (Excitonic absorption peak ~ 880 nm) WBG top cell is synergistically paired with a 0.95 eV (1300 nm) NBG bottom cell. The subcells are connected by an optimized interconnection layer (ICL) composed of 1,2-ethanedithiol-capped PbS QDs (PbS-EDT)/self-assembled monolayers (SAMs)/Au/zinc oxide (ZnO) [14]. To ensure matched current density and high overall performance, the top cell was fabricated to be thin and semi-transparent, while the bottom cell was thick and opaque. However, those top cells are susceptible to nanoscale morphological imperfections and pinholes, increasing the risk of damage during subsequent layer deposition. The chemically aggressive nature of EDT and its strong chelating properties allow it to partially penetrate into the underlying mixed-halide (PbI_2 and $PbBr_2$)-capped PbS QD (PbS-IBr) absorber layer, modifying its surface chemistry and potentially introducing interfacial defects [15–17]. Additionally, ZnO sputtering with high-energy ions can further compromise layer integrity [18]. The above chemical and physical damage could directly reduce TSC performance.

Several strategies have been explored in SJSCs to protect the PbS-IBr layer from the chemical aggressiveness of EDT. Milder short-chain alternatives, such as 2-mercaptoethanol (ME) [19] and malonic acid (MA) [20] have been used as substitutes for the EDT ligand. Nevertheless, the consistent use of EDT continues to deliver superior benchmark performance [21]. Attempts to employ interfacial modifiers such as polyethyleneimine (PEIE) [22] and poly (methacrylic acid) (PMAA) [23] have been hindered by their insulating nature and reactive groups, which can increase resistance and promote ligand displacement. On the other hand, in all-PbS QD TSCs, a robust electron transport layer (ETL) for the NBG bottom cell, such as sputtered ZnO [24–26], is preferred to shield underlying sensitive layers, as solution-processed ZnO has proven less effective [27,28]. The introduction of Poly[bis(4-phenyl) (2,4,6-trimethylphenyl) amine] (PTAA) and self-assembled monolayers (SAMs), such as 4PADCB, at the PbS-EDT/Au interface has led to improved efficiency but has demonstrated limited protection for the vulnerable PbS-IBr layer [14,29]. Ultimately, protecting the absorber layer of the top subcell from chemical and physical damage remains a significant challenge in the design of all-PbS QD TSCs.

Herein, we introduced a specialized p-type interlayer, chlorinated benzodithiophene-*alt*-dithienobenzothiadiazole copolymer, D18-Cl. The polymer's extended conjugation, arising from its sp^2-hybridized aromatic rings, ensures efficient delocalization and charge-carrier transport along the chain. Functionally, D18-Cl provides a dual-passivation scheme: the polymer backbone supplies sulfur atoms to heal anion vacancies, and its chlorine terminations coordinate with dangling bonds on unsaturated Pb sites. This strategy of interface modification with D18-Cl raises the valence-band maximum (VBM), thereby providing a graded pathway for holes and reducing the interfacial energy barrier. Moreover, an ultrathin D18-Cl interlayer may shield the PbS-IBr surface from the EDT solution, suppressing intermixing or damage to the WBG absorber layer. As a result of this comprehensive interfacial healing, the D18-Cl-based semitransparent top cell achieved a PCE of 10.36%, while the control achieved 7.82%. The corresponding tandem devices achieved a PCE of 13.148% (control: 11.84%).

2 Results and discussion

2.1 Bonding mechanism of the D18-Cl to PbS-IBr layer

Figure 1a schematically shows the WBG PbS-IBr thin film as the top-cell absorber layer deposited on the glass/ITO/ZnO substrate. The WBG PbS QDs are typically less than 5 nm in size, have a high surface-to-volume ratio, and contain sulfur vacancies induced from Pb-rich growth conditions [30]. Moreover, during the solution-phase ligand exchange of mixed lead halides (PbI_2 and $PbBr_2$) to PbS QDs, the surface remains partially passivated, leaving some unsaturated Pb sites. These sulfur vacancies and unsaturated Pb sites act as trap centers for charge carriers at the PbS-IBr/PbS-EDT interface. Additionally, they are highly reactive with oxygen and readily form oxides when exposed to air during subsequent layer deposition [9,10]. To address these challenges, the top-cell PbS-IBr absorber layer was post-treated by spin-coating a dilute D18-Cl solution (1 mg mL^{-1}), thereby forming an ultrathin interfacial modification layer at the PbS-IBr/PbS-EDT interface prior to HTL deposition. D18-Cl is a π-conjugated donor polymer semiconductor, widely used as an efficient hole-transport material, whose delocalized backbone enables hole transport. The utilized QD absorption spectra, top cell image, and TSC device structure are shown in Fig. S1.

To investigate the bonding mechanism of D18-Cl with PbS-IBr, Fourier transform infrared (FTIR) spectroscopy has been performed on D18-Cl, the bare PbS-IBr layer, and the PbS-IBr layer modified with D18-Cl (PbS-IBr/D18-Cl), as shown in Figs. 1b and 1c. In the fingerprint region of the

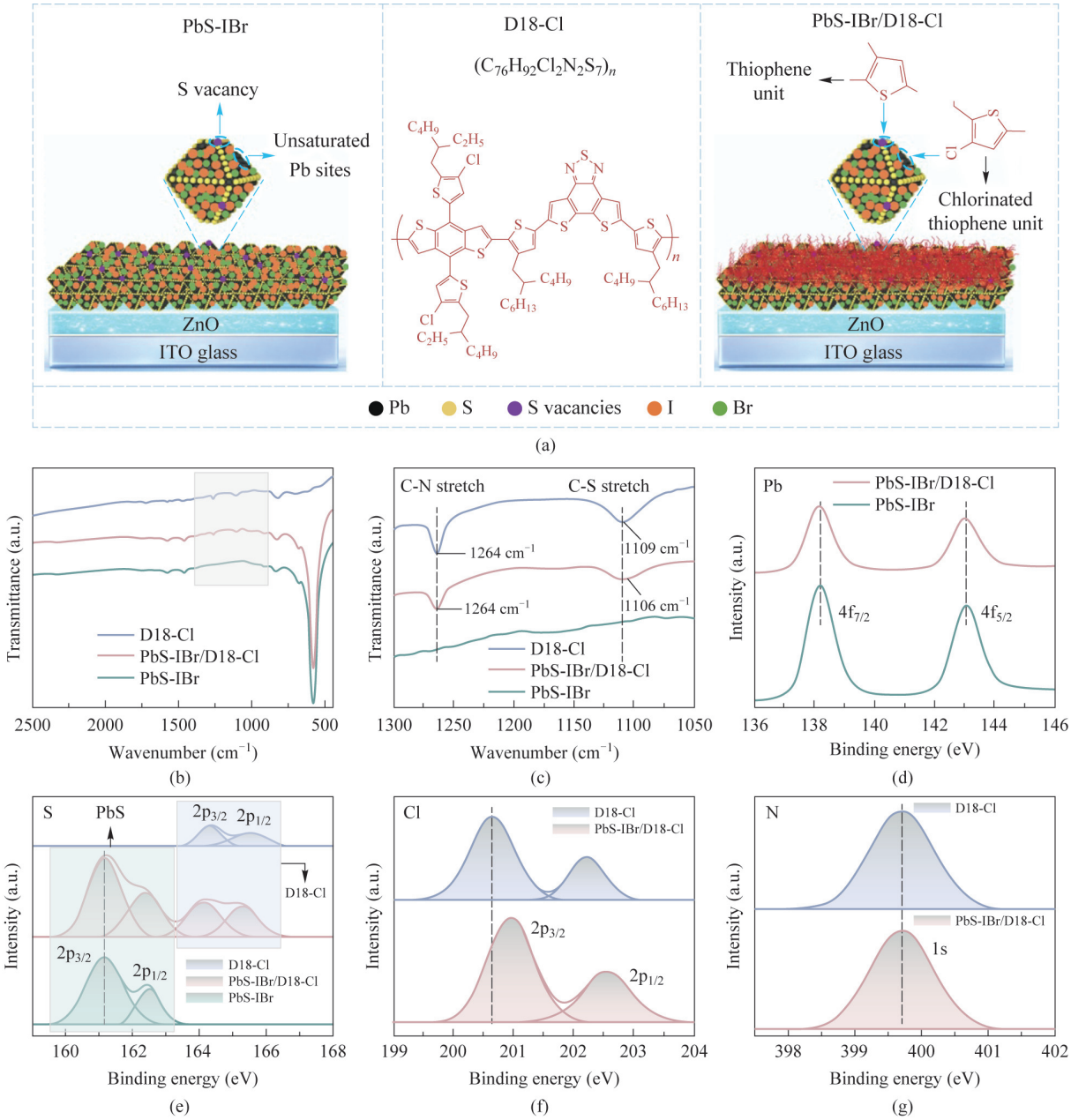

Fig. 1 (a) Schematic illustration of the fabrication process showing the sequential deposition of the WBG PbS QDs absorber layer, followed by surface modification treatment using the D18-Cl [32]. (b, c) Fourier-transform infrared (FTIR) spectroscopy analysis comparing the molecular vibrations in D18-Cl, bare (unmodified) PbS absorber film, and D18-Cl-modified absorber film. (d–g) X-ray photoelectron spectroscopy (XPS) analysis of the chemical composition and bonding states in D18-Cl, bare absorber, and modified films, showing core-level spectra for (d) lead (Pb 4f), (e) sulfur (S 2p), (f) chlorine (Cl 2p), and (g) nitrogen (N 1s).

spectra, two peaks were observed in both the D18-Cl and PbS-IBr/D18-Cl films in the range of 1000–1300 cm^{-1}, while no peaks were observed in this range for the PbS-IBr film. The peak at 1264 cm^{-1} corresponds to the C–N stretching vibration of D18-Cl and appears at the same position in both the D18-Cl and PbS-IBr/D18-Cl films, as shown in Figs. 1c and S2. However, the C–S stretching peak at 1109.39 cm^{-1} shifts to a lower wavenumber (1106 cm^{-1}) in the PbS-IBr/D18-Cl film. This red shift suggests a modified sulfur electronic environment upon contact with the PbS-IBr surface, consistent with interfacial interactions between thiophene sulfur atoms and undercoordinated surface sites.

To further evaluate the interaction between D18-Cl and PbS-IBr, X-ray photoelectron spectroscopy (XPS) analysis was performed. The Pb 4f core-level peaks are observed in

both the PbS-IBr and PbS-IBr/D18-Cl thin films, as shown in Fig. 1d and Tables S1–S4. In the PbS-IBr/D18-Cl film, the peak shifted to lower binding energy (138.15 eV) compared with the PbS-IBr film (138.25 eV). A slight shift of 0.1 eV toward lower binding energy suggests increased electron density and a modified local electrostatic environment around surface Pb atoms, indicating electronic coupling between D18-Cl and the PbS-IBr surface. Figure 1e shows the S 2p peaks, in which the PbS-IBr film has a peak centered at 161.25 eV that belongs to the S atom in PbS. In the pure D18-Cl film, the peak at 164.31 eV corresponds to the S atoms of the thiophene rings. In the PbS-IBr/D18-Cl film, both S element peaks from the PbS at 161.25 eV and from the thiophene ring at 164.31 eV are present, indicating the successful deposition of D18-Cl on the PbS-IBr layer. Figure 1f shows the binding energies of Cl for the D18-Cl and PbS-IBr/D18-Cl films. The binding energy of Cl in D18-Cl is 200.96 eV, which shifts to higher energy (201.15 eV) in the PbS-IBr/D18-Cl thin film. This shift of 0.19 eV toward the higher binding energy indicates interfacial charge redistribution involving the chlorine-containing moieties of D18-Cl and surface sites of PbS-IBr. Such behavior may arise from partial coordination, local dipole formation, or adsorption-induced electronic polarization at the interface. Figure S3 shows that the binding energies of halide ions (I and Br) in the bare absorber and modified films remain unchanged, indicating that no halide has been displaced after D18-Cl deposition, demonstrating its non-destructiveness toward surface atoms. The N peak observed in the pristine D18-Cl and modified films shows no noticeable change in binding energy, as shown in Fig. 1g and Tables S1–S4, indicating the chemical stability of the conjugated polymer [31].

2.2 Systematic analysis of the bare and modified absorber films

To further investigate the effect of D18-Cl on the PbS-IBr layer, PbS-IBr and PbS-IBr/D18-Cl thin films were characterized and analyzed in detail. Scanning electron microscopy (SEM) analysis was conducted to examine the surface morphology of the PbS-IBr and PbS-IBr/D18-Cl thin films, as shown in Figs. 2a and 2b. The PbS-IBr film demonstrates a predominantly uniform and continuous morphology, with only a few localized dark features, while the PbS-IBr/D18-Cl thin film is free from such localized dark features. To analyze the localized dark features in the PbS-IBr layer (circled area in Fig. 2a), we have performed energy dispersive X-ray (EDX) spectroscopy analysis for surface, as shown in Figs. 2c and S4. The observed decrease in Pb, S, and I signal is attributed to isolated, void-like coating defects that may arise from solvent evaporation kinetics, or local heterogeneity in QD packing during film formation. The increased O and Zn signals are explained by electron-beam penetration into the ZnO layer at those voids. To further confirm the quality of the thin films, atomic force microscopy (AFM) analysis was performed, as shown in Fig. S5. The needle-like or fibrillar morphology observed in PbS-IBr/D18-Cl films results from the intrinsic self-assembly behavior of D18-Cl. The extended conjugated backbone of D18-Cl promotes strong π–π stacking and the formation of nanofibrillar domains, as reported previously [32]. This fibrillar network is expected to facilitate interfacial charge transport and suppress recombination, thereby enhancing device performance. Moreover, the modified thin film exhibited a lower average surface roughness (R_q) of 1.1 nm than the pristine film (1.5 nm).

Ultraviolet photoelectron spectroscopy (UPS) measurements were performed for both films, as shown in Figs. 2d and 2e. The Fermi level calculated for the PbS-IBr/D18-Cl thin film is 4.40 eV, compared to 4.48 eV for the pristine PbS-IBr thin film. Figure 2f presents the energy band diagrams of the bare absorber and the modified thin films. The band energies derived from the UPS data clearly show that the highest occupied molecular orbital (HOMO) level of the modified film shifts upward by 0.16 eV, from 5.52 eV for the bare absorber layer to 5.36 eV. This upward shift in the HOMO level reduces the hole-injection barrier at the PbS-IBr/PbS-EDT interface. Thus, D18-Cl incorporation forms a π-conjugated, hole-selective interlayer that establishes an energetically graded hole-transport pathway and promotes hole extraction from the absorber (Fig. S6). Figures 2g and 2h show the surface potential distribution using Kelvin probe force microscopy (KPFM). The PbS-IBr/D18-Cl film exhibits a higher average surface potential of 471.975 mV compared to 255.583 mV for the PbS-IBr thin film. This increase in average surface potential is consistent with the UPS-derived upward shift in the Fermi level.

Photoluminescence (PL) analysis was performed to evaluate charge recombination and transfer, as shown in Fig. 2i. The PbS-IBr and PbS-IBr/D18-Cl thin films were deposited on the ZnO/ITO glass substrate for PL analysis. The PbS-IBr/D18-Cl thin film exhibited considerable PL quenching compared to the PbS-IBr thin film, attributed to the p-type nature of D18-Cl, which facilitates charge transfer at the interface. The photoluminescence quantum yield (PLQY) of PbS-IBr and PbS-IBr/D18-Cl was measured, and the quasi-Fermi level splitting (QFLS) values were calculated, as shown in Fig. S7. The PLQY of the PbS-IBr/D18-Cl film decreased to 0.112% compared with 0.137% for the PbS-IBr film. The calculated QFLS value of the PbS-IBr/D18-Cl film is 1.08 eV compared to 1.09

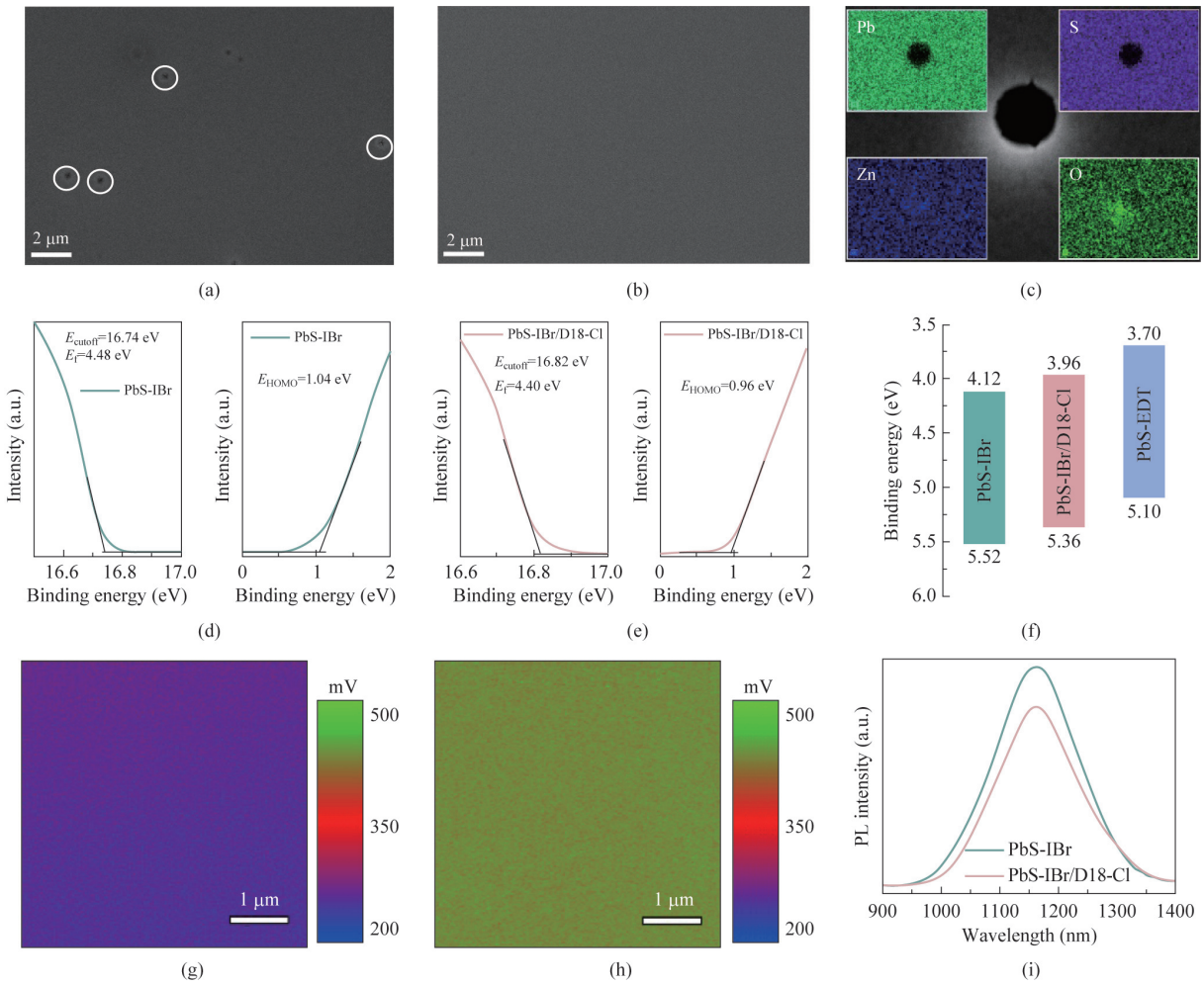

Fig. 2 Comprehensive electronic, morphological, and optical characterization of PbS-IBr films with and without D18-Cl modification. (a, b) Scanning electron microscopy (SEM) images showing the surface morphology of (a) PbS-IBr and (b) PbS-IBr/D18-Cl films. (c) Energy-dispersive X-ray (EDX) spectroscopy elemental composition analysis of the PbS-IBr thin film. (d, e) Ultraviolet photoelectron spectroscopy (UPS) measurements were used to determine the highest occupied molecular orbital (HOMO) energy level and Fermi energy level for (d) PbS-IBr control film and (e) D18-Cl-modified PbS-IBr film. (f) Schematic energy band alignment diagram constructed from UPS-derived energy levels, illustrating the electronic structure modification. (g, h) Kelvin probe force microscopy (KPFM) surface potential mapping of (g) PbS-IBr and (h) PbS-IBr/D18-Cl films. (i) Photoluminescence (PL) emission spectra comparing the radiative recombination characteristics of PbS-IBr and PbS-IBr/D18-Cl thin films.

eV for the PbS-IBr film. The observed reductions in PL, PLQY, and QFLS in the PbS-IBr/D18-Cl bilayer are attributed to efficient interfacial hole extraction rather than to increased recombination losses. Specifically, hole transfer from PbS-IBr to the p-type D18-Cl decreases the steady-state carrier population within the absorber, leading to the anticipated decreases in PL intensity and QFLS.

To distinguish the effects of defect passivation from those of charge extraction, PL measurements were performed on complete devices without back electrodes (Fig. S8). D18-Cl-modified samples exhibited substantially higher PL intensity compared to the pristine sample, indicating that D18-Cl effectively passivates non-radiative surface traps. Consequently, the PL quenching observed in the standard bilayer configuration (Fig. 2i) can be attributed to improved charge extraction rather than to increased non-radiative recombination. This enhanced extraction accounts for the observed improvements in both J_{sc} and V_{oc} in the devices, as explained in the coming sections [31,33].

2.3 Photovoltaic performance and carrier dynamics of semitransparent WBG PbS devices

To conduct a detailed analysis of D18-Cl over the PbS-IBr layer, we fabricated complete devices and measured various properties to assess its effect on device performance. Two device architectures were examined: control devices with the structure ITO glass/ZnO/PbS-IBr/PbS-EDT/Au

and D18-Cl devices with the structure ITO glass/ZnO/PbS-IBr/D18-Cl/PbS-EDT/Au. Cyclic voltammetry ($C-V$) analysis was performed to determine the built-in potential (V_{bi}), as shown in Fig. 3a. The V_{bi} was calculated using Eq. (1) [34]

$$\frac{1}{C^2} = \frac{2(V_{bi} - V)}{A^2 e \varepsilon_o \varepsilon_r N}, \tag{1}$$

where C is the capacitance, V_{bi} is the built-in potential, V is the applied voltage, A is the area of the junction, e is the elementary charge, ε_o is the permitivity of vacuum, ε_r is the relative permitivity of the material, and N is the doping concentration. The D18-Cl-based devices exhibited a higher V_{bi} (0.54 V) than the control devices (0.51 V), thereby facilitating enhanced charge separation and extraction. Figures 3b and 3c show the depletion width (W_d) calculated using the parallel-plate capacitor model in Eq. (2) [35]

$$W_d = \frac{\varepsilon_o \varepsilon_r A}{C}. \tag{2}$$

The W_d for the D18-Cl-based device was estimated at 72.8 nm, significantly larger than that of the control device (59.0 nm). Given that the absorber film was approximately 140 nm thick, the D18-Cl-based device is expected to exhibit greater depletion, thereby facilitating more efficient carrier separation and transport.

The drive-level capacitance profiling (DLCP) measurement was used to determine the bulk doping concentration (N_{DLCP}). In contrast, the interface doping concentration was calculated by subtracting N_{DLCP} from the doping concentra-

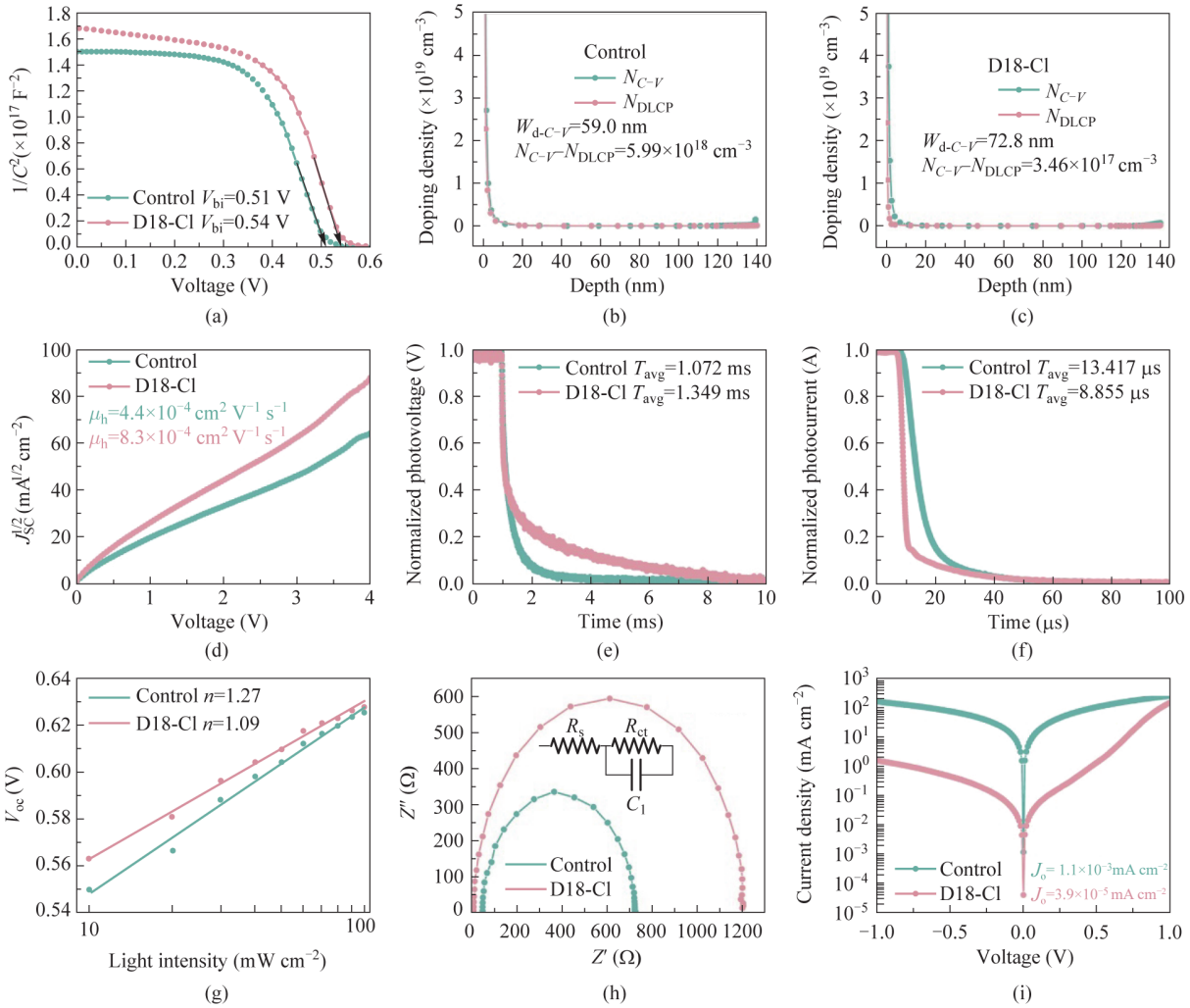

Fig. 3 Electrical characterization of control and D18-Cl-based devices. (a) Capacitance–voltage ($C-V$) characteristics. (b, c) Drive-level capacitance profiling (DLCP) analysis of (b) control and (c) D18-Cl-based devices. (d) Hole mobility determination from space-charge-limited current (SCLC) measurements. (e) Transient photovoltage (TPV) decay graph. (f) Transient photocurrent (TPC) decay graph. (g) Open-circuit voltage (V_{oc}) dependence on light intensity. (h) Electrochemical impedance spectroscopy (EIS) analysis. (i) Dark current density–voltage ($J-V$) curves.

tion obtained from $C-V$ data (N_{C-V}), as N_{C-V} is sensitive to both bulk and interface defects. Figures 3b and 3c show that the interface defect concentration for the D18-Cl-based sample (3.46×10^{17} cm^{-3}) is significantly lower than that of the control (5.99×10^{18} cm^{-3}). This reduction in interface-defect concentration is attributed to the D18-Cl treatment, which passivates defects and enhances charge extraction. Figure 3d presents the hole mobility of both control and D18-Cl-based devices, calculated from hole-only devices (ITO Glass/PEDOT: PSS/PbS-IBr/PbS-EDT/Au and ITO Glass/PEDOT: PSS/PbS-IBr/D18-Cl/PbS-EDT/Au) using the Mott–Gurney law in Eq. (3) [36]

$$J = \frac{9\varepsilon_o\varepsilon_r\mu V^2}{8L^3}, \tag{3}$$

where ε_r is the relative dielectric constant (18 for PbS QDs), ε_o is the vacuum permittivity, L is the thickness of the QD films (140 nm), V is the applied voltage, and J is the current density, respectively. After incorporating the D18-Cl layer, hole mobility increased from 4.4×10^{-4} cm^2 V^{-1} s^{-1} to 8.3×10^{-4} cm^2 V^{-1} s^{-1}, indicating faster, more efficient hole extraction [32,37].

Transient photovoltage (TPV) analysis was performed to determine the carrier lifetime, as shown in Fig. 3e. The carrier average lifetime (T_{ave}), calculated from the first exponential decay fit, was 1.349 ms for the D18-Cl-based sample, which is higher than that of the control (1.072 ms). Transient photocurrent (TPC) analysis was performed to determine carrier transport dynamics, as shown in Fig. 3f. The corresponding transport time (T_{ave}) for the D18-Cl-based sample was 8.855 μs compared to 13.417 μs for the control. In the D18-Cl-based sample, charges were collected efficiently before recombination. The diffusion length (L_D) was calculated from the TPC data using Eq. (4) [38]

$$L_D = \sqrt{\frac{\mu k_B T \tau}{q}}, \tag{4}$$

where L_D is diffusion length, μ is hole mobility, k_B is the Boltzmann constant, T is the temperature, τ is the average lifetime, and q is the elementary charge. The diffusion length calculated for the D18-Cl-based sample is 138 nm, and for the control sample is 124 nm. Considering both the depletion width and the diffusion length, charge transport primarily arises from the combined effects of drift and diffusion. The increased diffusion length mainly reflects improved carrier lifetime and transport quality.

To analyze the recombination loss mechanism of photocarriers, light-intensity-dependent current density–voltage (J–V) measurements were performed. The dependence of open circuit voltage (V_{oc}) on light intensity is described by Eq. (5) [39]

$$V_{oc} = \frac{nk_B T}{q\ln(I)}, \tag{5}$$

where n is an evaluation factor, k_B is the Boltzmann constant, T is the temperature in Kelvin, and I is the light intensity. From linear slope fitting (Fig. 3g), we obtained n values of 1.27 and 1.09 for the control and D18-Cl-based devices, respectively, indicating suppression of Shockley–Read–Hall (SRH) recombination in the D18-Cl-based device. Figure 3h shows the Nyquist plots of the control and D18-Cl-based samples obtained from electrochemical impedance spectroscopy (EIS). Incorporating D18-Cl decreased the series resistance from 51.87 Ω cm^2 to 13.05 Ω cm^2 and increased the shunt resistance from 725.92 Ω cm^2 to 1196.6 Ω cm^2. Higher R_{sh} after D18-Cl treatment results from suppressed leakage at the PbS-IBr/PbS-EDT interface due to reduced trap-assisted recombination and better interfacial coverage. Improved contact selectivity further enhances hole extraction and suppresses electron leakage, increasing shunt resistance and overall improved device performance. Figure 3i presents the dark J–V curves. The dark saturation current for the D18-Cl-based device was 3.93×10^{-5} mA cm^{-2}, one order of magnitude lower than that of the control device (1.14×10^{-3} mA cm^{-2}), indicating that the D18-Cl-based devices suppress leakage current, thereby improving diode quality.

Figure 4a shows the schematic diagram of the semi-transparent WBG PbS QDs SJSC used as the top cell in TSCs. The diagram illustrates the post-treatment of the PbS-IBr layer with a 1 mg/mL D18-Cl solution. Figure 4b presents the $J-V$ curves and photovoltaic parameters for both control and D18-Cl-treated devices. The incorporation of D18-Cl significantly improved all key performance metrics: V_{oc} increased from 0.613 V to 0.635 V, short-circuit current density (J_{sc}) increased from 19.946 mA cm^{-2} to 24.574 mA cm^{-2}, fill factor (FF) increased from 63.882% to 67.471%, and PCE increased from 7.820% to 10.369%. Table S5 compares the top-performing device from this work with previously published results, listing the bandgap, absorber layer thickness, and device performance of the top cells. Our D18-Cl-modified top cell device achieved the highest PCE reported to date for this device architecture.

As shown in the external quantum efficiency (EQE) spectra (Fig. 4c), the D18-Cl-based devices exhibit higher quantum efficiency, with an integrated J_{sc} of 22.70 mA cm^{-2}, compared with the control devices (18.24 mA cm^{-2}). Based on the statistical analysis of 20 batch devices shown in Fig. 4d, the average values of key parameters for D18-Cl-treated devices are higher than those for control devices. To optimize device performance, the effect of variable D18-Cl concentrations (0.25–2 mg mL^{-1}) was evaluated. Initially, increasing the D18-Cl concentration improves de-

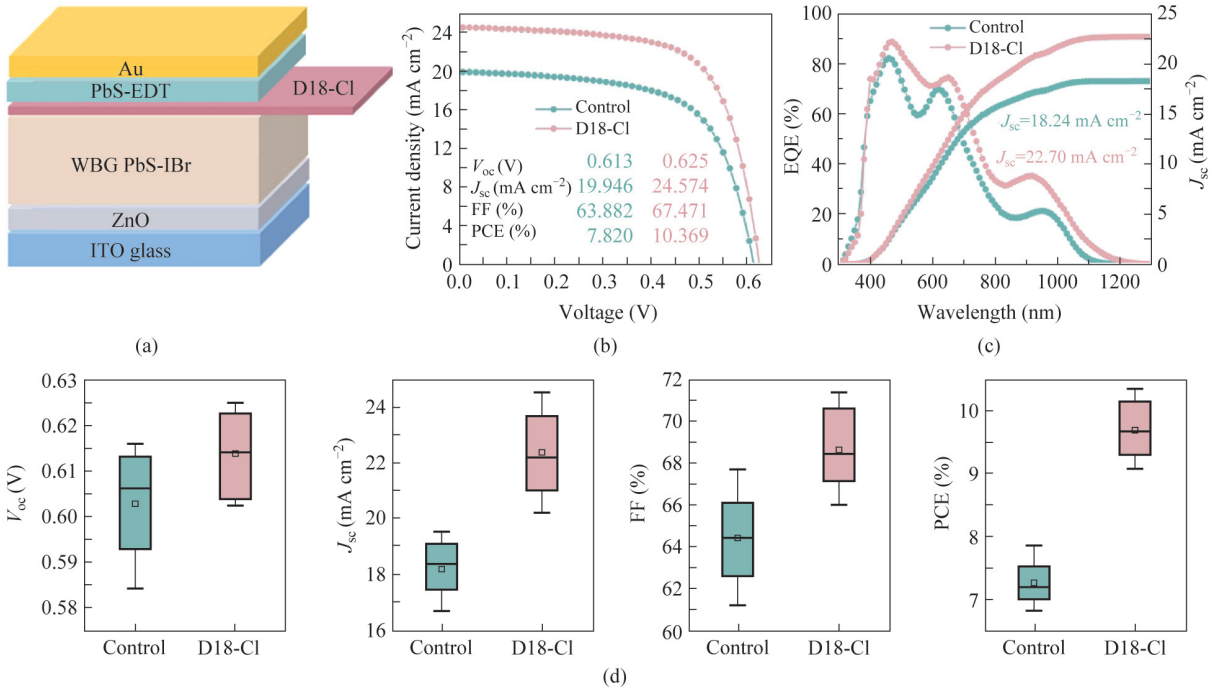

Fig. 4 Top cell characterization of control and D18-Cl-based devices. (a) Schematic diagram of the top cell device architecture. (b) Current density−voltage (J−V) curves under illumination. (c) External quantum efficiency (EQE) spectra with integrated photocurrent density values. (d) Box plots of key photovoltaic parameters.

vice performance, with an optimal value at 1 mg mL^{-1}. Further increasing the concentration reduces device performance, as shown in Fig. S9. This decline in performance at concentrations above 1 mg mL^{-1} may be attributed to the accumulation of unreacted D18-Cl at the interface, which increases resistance. Alternatively, a separate D18-Cl layer may form, disrupting the band alignment at the interface.

2.4 Optoelectronic performance of tandem solar cells

Figure 5a shows a schematic of the TSC architecture. A semitransparent top cell modified with D18-Cl is connected to an opaque bottom cell via optimized interconnecting layers (ICLs) comprising PbS-EDT/SAMs/Au/ZnO, as reported in our previous work [14]. Cross-sectional scanning electron microscopy (SEM) was used to quantify the thickness of each layer, shown in Figs. 5b and S10. In the bottom cell of the TSCs, 0.95 eV PbS QDs (Fig. S11) were used as the absorber. The bottom cell SJSC with a standard structure of Glass/ITO/ZnO/PbS-IBr/PbS-EDT/Au achieved a PCE of 10.573% (V_{oc} = 0.483 V, J_{sc} = 33.628 mA cm^{-2}, FF = 65.088%) (Fig. S12). The performance ranges of the bottom-cell SJSC and the integrated J_{sc} values calculated from the EQE data are provided in Figs. S13 and S14.

By combining the bottom and top cells, the control tandem devices achieved a PCE of 11.84% (V_{oc} = 1.068 V, J_{sc} = 16.570 mA cm^{-2}, FF = 66.920%). Applying the D18-Cl-based top cell, the champion TSC achieved a significantly higher PCE of 13.16%, with a V_{oc} of 1.074 V, J_{sc} of 16.731 mA cm^{-2}, and FF of 73.127%, as shown in Fig. 5c. The distributions of the J-V parameters are illustrated in Fig. S15 for control and D18-Cl-treated tandem devices from 10 batches (2 highest-performing devices per batch). The average V_{oc}, J_{sc}, FF, and PCE values in the D18-Cl tandem devices were significantly higher than those of the control devices. Furthermore, the narrow distribution of PCE (12.7 ± 0.45%) indicated the high reproducibility of the D18-Cl effect. The EQE analysis of the D18-Cl tandem devices is presented in Fig. 5d. The TSC EQE spectra show > 80% response in the top cell and broad photoresponse in the bottom cell. The summed EQE approaches 90%, and matched photocurrents (16.36 mA cm^{-2} and 16.16 mA cm^{-2}) for the top and bottom cells confirm excellent current balance.

Figure 5e demonstrates the operational stability of the TSC. The tandem devices were encapsulated with a cover glass sealed with ultraviolet-curable adhesive and tested under continuous 1-sun-equivalent white LED illumination (AM 1.5G spectrum) at ambient temperature and humidity. The encapsulated device retains more than 90% of its initial PCE after 500 h of continuous MPPT. Figure 5f shows the storage stability of the devices in air at approxi-

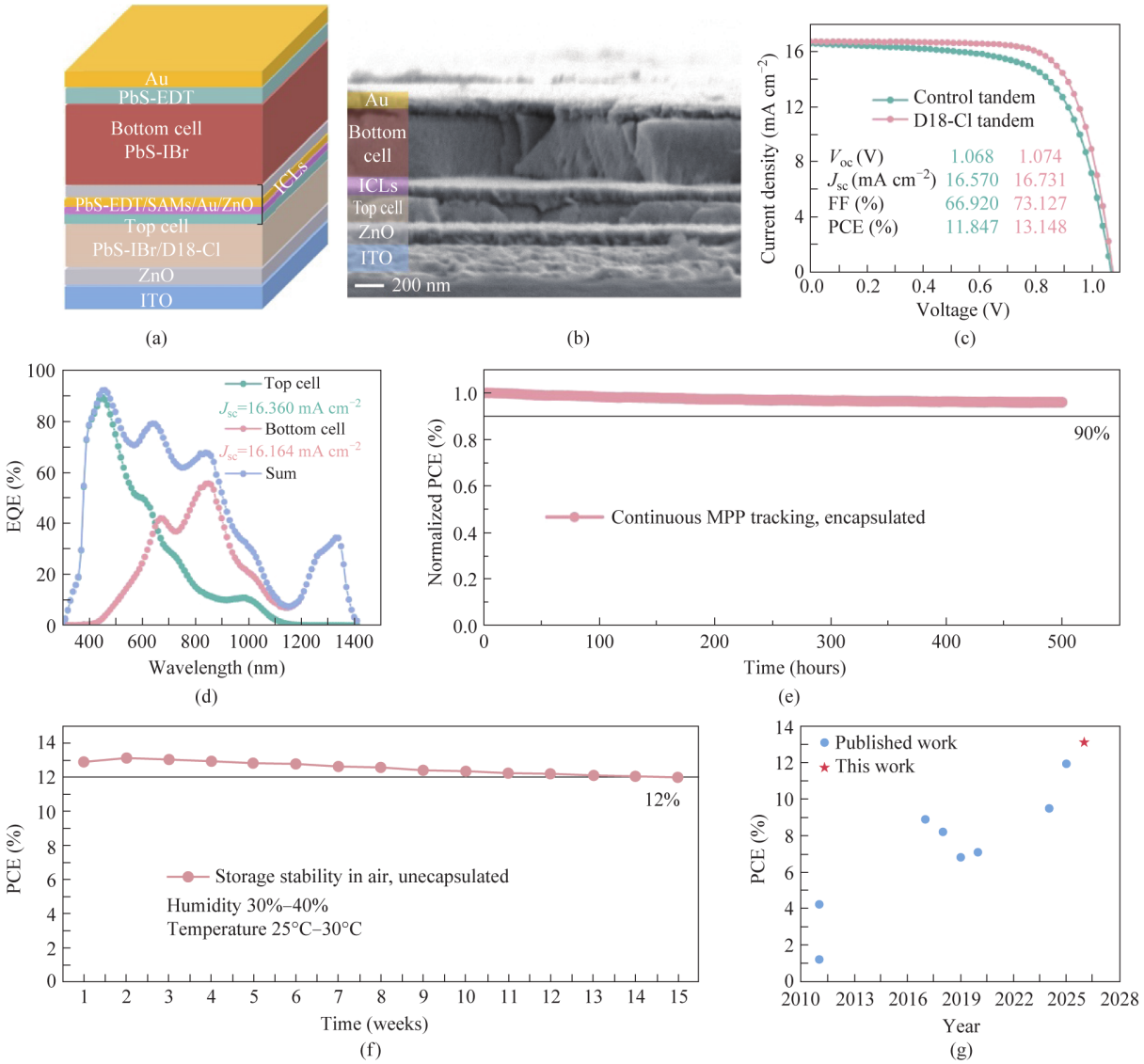

Fig. 5 Tandem device architecture, performance, and stability characterization. (a) Schematic diagram of the tandem device architecture. (b) Cross-sectional SEM image of the tandem device. (c) Current density−voltage (J–V) curves under illumination for control and D18-Cl-based tandem devices. (d) External quantum efficiency (EQE) spectra of the champion tandem device. (e) Maximum power point tracking (MPPT) stability of the D18-Cl-based tandem device. (f) Storage stability of the champion tandem device under ambient air conditions. (g) Comparison of power conversion efficiency (PCE) achieved in this work with previously published results.

mately 30%–40% relative humidity and a temperature of 25°C–30°C. Device performance was tracked weekly, and the highest weekly PCE was plotted. Initially, the device PCE increased from 12.9% to 13.148%, then declined each week. This slight improvement in PCE may be attributed to the oxidation of EDT in air. After more than 3 months of air storage, the devices retain more than 90% of their initial PCE, indicating high stability in air. Figures 5g, S16, and Table S6 compare the results achieved in this work with previously published results. The FF of 73% is higher than that reported in all previous publications. For the first time, PbS QD TSC achieved an FF above 70%. This improvement in FF reflects the enhanced charge-extraction capabilities of the modified devices. The champion device achieved the highest PCE of 13.148%, representing an absolute increase of 1.2% compared with recently published work.

3 Conclusion

In conclusion, we successfully modified the PbS-IBr/PbS-EDT interface with D18-Cl and fabricated a WBG semi-transparent device that serves as the top cell in all PbS QD

2T TSCs. This interface coating could bind to the undercoordinated Pb^{2+} and passivate sulfur vacancies. The D18-Cl also protects the absorber layer from chemical and physical damage during TSC fabrication and provides a graded pathway to enhance charge extraction. As a result, the modified semi-transparent top cell achieved a PCE of 10.36% compared to the control (7.82%). By integrating this semitransparent cell into TSCs, we achieved a PCE of 13.148%, the highest reported to date for all-PbS QD TSCs. This is an absolute 1.2% PCE increase compared to our recent published work (11.95%). The modified TSC devices retain more than 90% of their initial PCE after 500 h of MPPT operation and 15 weeks of air storage.

Electronic Supplementary Material The supplementary content includes PbS QDs synthesis, device fabrication, and characterization processes, Figs. S1−S15, and Tables S1−S6. These encompass spectrally matched PbS tandem cells, raw FTIR data, XPS data, AFM images, EDX elemental analysis, a schematic energy band diagram, PL spectra of complete devices, PLQY and QFLS data, box plots of D18-Cl-dependent device metrics, a cross-sectional SEM image, absorption spectra of 1300 nm QDs, a schematic diagram of the bottom cell SJSC, the *J*−*V* curve of the bottom cell SJSC, box plots of bottom cell SJSC parameters, the EQE curve of the bottom cell SJSC, box plots comparing control and D18-Cl tandem devices, FF comparison chart, and Tables S1−S4 detailing XPS data, Table S5 reporting WBG PbS top cell performance from prior work, and Table S6 presenting tandem devices performance from prior work.

Supplementary Information The online version contains Electronic Supplementary Material available at https://doi.org/10.2738/foe.2026.0024.

Acknowledgements This work was supported by the National Natural Science Foundation of China (Grant Nos. 62374065, 62574096), the Wuhan Key Research and Development Program (2025010602030106), Project for Building a Science and Technology Innovation Center Facing South Asia and South-east Asia (202403AP140015), the Innovation Project of Optics Valley Laboratory (Nos. OVL2021BG008, OVL2024ZD002), Shenzhen Science and Technology Program (JCYJ20250604190827037). The authors thank Engineer Jun Su from the Center of Optoelectronic Micro and Nano Fabrication and Characterizing Facility, WNLO of HUST, for the support in the SEM test. The authors also thank the Analytical and Testing Center and the Optical and Electronic Information School of HUST for their support in providing facilities for sample measurements.

Author contribution **S. Ali:** Methodology, investigation, formal analysis, data curation, writing original draft. **X. Zhao:** Methodology, investigation. **M. Li:** Software, resources, investigation. **R. Gao:** Resources, methodology. **T. Ma:** Resources, data curation. **Y. Li:** Resources, methodology. **G. M. G. Khalaf, M. Wang, and C. Cheng:** Methodology, investigation. **J. Zhang:** Resources, software. **H. Song:** Supervision, investigation, funding acquisition, data curation. **J. Tang:** Resources, funding acquisition. All authors have approved the final manuscript.

Declarations

Competing interests All the contributing authors report no conflicts of interest in this work.

Availability of data and materials All data needed to support the conclusions in the paper are presented in the manuscript and the Electronic Supplementary Material. Additional data related to this paper may be requested from the corresponding author upon request.

Use of AI statement None.

References

1. Wen, J., Hu, H., Chen, C., McMeekin, D.P., Xiao, K., Lin, R., Liu, Y., Snaith, H.J., Tang, J., Paetzold, U.W., Tan, H.: Present status of and future opportunities for all-perovskite tandem photovoltaics. Nat. Energy **10**(6), 681–696 (2025)
2. Chen, W., Zhu, Y., Xiu, J., Chen, G., Liang, H., Liu, S., Xue, H., Birgersson, E., Ho, J.W., Qin, X., Lin, J., Ma, R., Liu, T., He, Y., Ng, A.M.C., Guo, X., He, Z., Yan, H., Djurišić, A.B., Hou, Y.: Monolithic perovskite/organic tandem solar cells with 23.6% efficiency enabled by reduced voltage losses and optimized interconnecting layer. Nat. Energy **7**(3), 229–237 (2022)
3. Yang, G., Deng, C., Li, C., Zhu, T., Liu, D., Bai, Y., Chen, Q., Huang, J., Li, G.: Towards efficient, scalable and stable perovskite/silicon tandem solar cells. Nat. Photonics **19**(9), 913–924 (2025)
4. Zhu, J., Lu, K., Li, J., Liu, Z., Ma, W.: Tandem solar cells based on quantum dots. Mater. Chem. Front **8**(7), 1792–1807 (2024)
5. Liu, C., Gao, H., Ou, W., Tan, H., Lin, R.: Light management in monolithic all-perovskite tandem solar cells. Light Sci. Appl **15**(1), 56 (2026)
6. Yang, X., Ma, T., Hu, H., Ye, W., Li, X., Li, M., Zhang, A., Ge, C., Sun, X., Zhu, Y., Yan, S., Yan, J., Zhou, Y., Li, Z., Chen, C., Song, H., Tang, J.: Understanding and manipulating the crystallization of Sn–Pb perovskites for efficient all-perovskite tandem solar cells. Nat. Photonics **19**(4), 426–433 (2025)
7. Brinkmann, K.O., Becker, T., Zimmermann, F., Kreusel, C., Gahlmann, T., Theisen, M., Haeger, T., Olthof, S., Tückmantel, C., Günster, M., Maschwitz, T., Göbelsmann, F., Koch, C., Hertel, D., Caprioglio, P., Peña-Camargo, F., Perdigón-Toro, L., Al-Ashouri, A., Merten, L., Hinderhofer, A., Gomell, L., Zhang, S., Schreiber, F., Albrecht, S., Meerholz, K., Neher, D., Stolterfoht, M., Riedl, T.: Perovskite–organic tandem solar cells with indium oxide interconnect. Nature **604**(7905), 280–286 (2022)
8. Li, M., Yan, J., Zhang, A., Zhao, X., Yang, X., Yan, S., Ma, N., Ma, T., Luo, D., Chen, Z., Li, L., Li, X., Chen, C., Song, H., Tang, J.: Vacuum-driven precrystallization enables efficient all-perovskite tandem solar cells. Joule **9**(4), 101825 (2025)

9. Fan, J.Z., Andersen, N.T., Biondi, M., Todorović, P., Sun, B., Ouellette, O., Abed, J., Sagar, L.K., Choi, M.J., Hoogland, S., de Arquer, F.P.G., Sargent, E.H.: Mixed lead halide passivation of quantum dots. Adv. Mater **31**(48), 1904304 (2019)
10. Khalaf, G.M.G., Li, M., Yan, J., Zhao, X., Ma, T., Hsu, H.Y., Song, H.: PbS colloidal quantum dots infrared solar cells: defect information and passivation strategies. Small Sci **3**(11), 2300062 (2023)
11. Tavakoli, M.M., Dastjerdi, H.T., Yadav, P., Prochowicz, D., Si, H., Tavakoli, R.: Ambient stable and efficient monolithic tandem perovskite/PbS quantum dots solar cells via surface passivation and light management strategies. Adv. Funct. Mater **31**(21), 2010623 (2021)
12. Ke, A., Ali, S., Gao, R., Shen, G., Zhao, X., Yan, J., Ma, T., Li, M., Liu, B., Hsu, H.Y., Chen, C., Tang, J., Song, H.: Two-terminal Sb_2S_3/PbS-QDs tandem solar cells with over 12% certificated efficiency utilizing bidentate additive strategy. Adv. Energy Mater **15**(39), e03358 (2025)
13. Chen, S., Zhao, X., Shen, G., Ke, A., Liu, B., Hsu, H.Y., Chen, C., Yang, P., Tang, J., Song, H.: All-inorganic Sb_2S_3-based two-terminal tandem solar cells enable over 10.9% efficiency employing a concise interconnection layer. J. Mater. Chem. A Mater. Energy Sustain **12**(29), 18148–18156 (2024)
14. Ali, S., Khalaf, G.M.G., Ke, A., Li, C., Zhao, X., Shen, G., Yan, J., Ishaq, M., Hsu, H.Y., Chen, C., Zhang, J., Song, H., Tang, J.: Interface modification enables 11.95%-efficient all-PbS-QDs tandem solar cells utilizing self-assembled monolayers. Sol. RRL **9**(24), e202500671 (2025)
15. Meng, X., Chen, Y., Yang, F., Zhang, J., Shi, G., Zhang, Y., Tang, H., Chen, W., Liu, Y., Yuan, L., Li, S., Wang, K., Chen, Q., Liu, Z., Ma, W.: Perovskite bridging PbS quantum dot/polymer interface enables efficient solar cells. Nano Res **15**(7), 6121–6127 (2022)
16. Wen, X., Gao, C., Ding, X., Shi, G., Yuan, X., Li, B., Yuan, L., Guo, J., Duan, C., Shen, Q., Ma, W., Liu, Z.: Double-side interfacial engineering of hole transport layer enables efficient and operationally stable colloidal quantum dot solar cells. Adv. Mater **37**(28), 2500562 (2025)
17. Khalaf, G.M.G., Fang, F., Zou, Y., Müller-Buschbaum, P., Chen, W.: Emerging hole transport layers for PbS quantum dot solar cells and photodetectors. J. Mater. Chem. A Mater. Energy Sustain **14**(15), 8537–8559 (2026)
18. Thiesbrummel, J., Peña-Camargo, F., Brinkmann, K.O., Gutiérrez-Partida, E., Yang, F., Warby, J., Albrecht, S., Neher, D., Riedl, T., Snaith, H.J., Stolterfoht, M., Lang, F.: Understanding and minimizing V_{OC} losses in all-perovskite tandem photovoltaics. Adv. Energy Mater **13**(3), 2202674 (2023)
19. Wang, C., Wu, Q., Wang, Y., Wang, Z., Li, H., Li, X., Chen, X., Wang, C., Liu, Y., Zhang, X.: P-type PbS quantum dot solar ink via hydrogen-bonding modulated solvation for high-efficiency photovoltaics. Adv. Funct. Mater **34**(18), 2315365 (2024)
20. Biondi, M., Choi, M.J., Ouellette, O., Baek, S.W., Todorović, P., Sun, B., Lee, S., Wei, M., Li, P., Kirmani, A.R., Sagar, L.K., Richter, L.J., Hoogland, S., Lu, Z.H., García de Arquer, F.P., Sargent, E.H.: A chemically orthogonal hole transport layer for efficient colloidal quantum dot solar cells. Adv. Mater **32**(17), 1906199 (2020)
21. Gui, Z., Wang, C., Wang, Y., Zhu, H., Li, H., Wang, Z., Li, X., Yang, S., Zhang, X., Liu, Y.: Boosting near-infrared utilization in PbS quantum dot solar cells via a back-interface chemical-bonding molecular buffer. Adv. Funct. Mater **36**(13), 16801 (2026)
22. Zhang, L., Chen, Y., Cao, S., Yuan, D., Tang, X., Wang, D., Gao, Y., Zhang, J., Zhao, Y., Yang, X., Lu, Z., Fan, Q., Sun, B.: Interfacial heterojunction enables highly efficient PbS quantum dot solar cells. Adv. Sci. (Weinh.) **11**(26), 2402756 (2024)
23. Ding, C., Wang, D., Liu, D., Li, H., Li, Y., Hayase, S., Sogabe, T., Masuda, T., Zhou, Y., Yao, Y., Zou, Z., Wang, R., Shen, Q.: Over 15% efficiency PbS quantum-dot solar cells by synergistic effects of three interface engineering: reducing nonradiative recombination and balancing charge carrier extraction. Adv. Energy Mater **12**(35), 2201676 (2022)
24. Bi, Y., Pradhan, S., Akgul, M.Z., Gupta, S., Stavrinadis, A., Wang, J., Konstantatos, G.: Colloidal quantum dot tandem solar cells using chemical vapor deposited graphene as an atomically thin intermediate recombination layer. ACS Energy Lett **3**(7), 1753–1759 (2018)
25. Shi, G., Wang, Y., Liu, Z., Han, L., Liu, J., Wang, Y., Lu, K., Chen, S., Ling, X., Li, Y., Cheng, S., Ma, W.: Stable and highly efficient PbS quantum dot tandem solar cells employing a rationally designed recombination layer. Adv. Energy Mater **7**(15), 1602667 (2017)
26. Wang, X., Koleilat, G.I., Tang, J., Liu, H., Kramer, I.J., Debnath, R., Brzozowski, L., Barkhouse, D.A.R., Levina, L., Hoogland, S., Sargent, E.H.: Tandem colloidal quantum dot solar cells employing a graded recombination layer. Nat. Photonics **5**(8), 480–484 (2011)
27. Gao, Y., Zheng, J., Chen, W., Yuan, L., Teh, Z.L., Yang, J., Cui, X., Conibeer, G., Patterson, R., Huang, S.: Enhancing PbS colloidal quantum dot tandem solar cell performance by graded band alignment. J. Phys. Chem. Lett **10**(19), 5729–5734 (2019)
28. Choi, J.J., Wenger, W.N., Hoffman, R.S., Lim, Y.F., Luria, J., Jasieniak, J., Marohn, J.A., Hanrath, T.: Solution-processed nanocrystal quantum dot tandem solar cells. Adv. Mater **23**(28), 3144–3148 (2011)
29. Mohamed Gomaa Khalaf, G., Zhao, X., Li, M., Li, C., Ali, S., Ma, T., Hsu, H.Y., Zhang, J., Song, H.: Efficient PbS quantum dots tandem solar cells through compatible interconnection layer. J. Energy Chem **98**, 47–57 (2024)
30. Xia, Y., Liu, S., Wang, K., Yang, X., Lian, L., Zhang, Z., He, J., Liang, G., Wang, S., Tan, M., Song, H., Zhang, D., Gao, J., Tang, J., Beard, M.C., Zhang, J.: Synthesis of highly monodisperse PbS quantum dots from ZnS nanorods for efficient infrared solar cells. Adv. Funct. Mater **30**(4), 1907379 (2020)
31. Shen, L., Song, P., Jiang, K., Zheng, L., Qiu, J., Li, F., Huang, Y., Yang, J., Tian, C., Jen, A.K.Y., Xie, L., Wei, Z.: Ultrathin polymer membrane for improved hole extraction and ion blocking in perovskite solar cells. Nat. Commun **15**(1), 10908 (2024)
32. Tang, X., Yang, C., Xu, Y., Xia, J., Li, B., Li, M., Zhou, Y., Jiang, L., Liu, H., Ma, K., Yu, Q., Dong, B., Liu, Y., Mohammed, O.F., Zheng, X.: Enhancing the efficiency and stability of perovskite solar cells via a polymer heterointerface bridge. Nat. Photonics **19**(7), 701–708 (2025)
33. Tang, J., Sargent, E.H.: Infrared colloidal quantum dots for photovoltaics: fundamentals and recent progress. Adv. Mater **23**(1), 12–29 (2011)
34. Tang, J., Brzozowski, L., Barkhouse, D.A.R., Wang, X., Debnath, R., Wolowiec, R., Palmiano, E., Levina, L., Pattantyus-Abraham, A.G., Jamakosmanovic, D., Sargent, E.H.: Quantum dot photovoltaics in the extreme quantum confinement regime: the surface-chemical origins of exceptional air- and light-stability. ACS Nano **4**(2), 869–878 (2010)
35. Zhang, Y., Wu, G., Ding, C., Liu, F., Liu, D., Masuda, T., Yoshino, K., Hayase, S., Wang, R., Shen, Q.: Surface-modified graphene oxide/lead sulfide hybrid film-forming ink for high-efficiency bulk nano-heterojunction colloidal quantum dot solar cells. Nano-Micro Lett **12**(1), 111 (2020)
36. Qin, J., Zhang, L., Zuo, C., Xiao, Z., Yuan, Y., Yang, S., Hao, F., Cheng, M., Sun, K., Bao, Q., Bin, Z., Jin, Z., Ding, L.: A

chlorinated copolymer donor demonstrates a 18.13% power conversion efficiency. J. Semicond **42**(1), 010501 (2021)
37. Zeng, A., Ma, X., Pan, M., Chen, Y., Ma, R., Zhao, H., Zhang, J., Kim, H.K., Shang, A., Luo, S., Angunawela, I.C., Chang, Y., Qi, Z., Sun, H., Lai, J.Y.L., Ade, H., Ma, W., Zhang, F., Yan, H.: A chlorinated donor polymer achieving high-performance organic solar cells with a wide range of polymer molecular weight. Adv. Funct. Mater **31**(33), 2102413 (2021)
38. Wang, Y., Lu, K., Han, L., Liu, Z., Shi, G., Fang, H., Chen, S., Wu, T., Yang, F., Gu, M., Zhou, S., Ling, X., Tang, X., Zheng, J., Loi, M.A., Ma, W.: In situ passivation for efficient PbS quantum dot solar cells by precursor engineering. Adv. Mater **30**(16), 1704871 (2018)
39. Shen, G., Ke, A., Chen, S., Ma, T., Ali, S., Li, M., Hsu, H.Y., Chen, C., Yang, P., Song, H., Tang, J.: Strong chelating additive and modified electron transport layer for 8.26%-efficient Sb_2S_3 solar cells. Adv. Energy Mater **15**(24), 2406051 (2025)

Salman Ali is a Ph.D. student at the Wuhan National Laboratory for Optoelectronics (WNLO), Huazhong University of Science and Technology, China. He obtained his master's degree from Abdul Wali Khan University Mardan (AWKUM), KP, Pakistan, in 2019. He joined WNLO in 2022 and is currently engaged in research on solar cells. His work primarily focuses on the synthesis of high-quality lead sulfide quantum dots and their application in single-junction and tandem solar cells to enhance device efficiency and stability.

Xinzhao Zhao is a Ph.D. student at the Wuhan National Laboratory for Optoelectronics, Huazhong University of Science and Technology, China. In 2021, he received his bachelor's degree from Zhengzhou University, China. Then he came to Huazhong University of Science and Technology to conduct research on optoelectronic devices. The main research direction is to construct efficient and stable quantum dot solar cells and all-perovskite tandem solar cells.

Mingyu Li obtained his Ph.D. degree from the Wuhan National Laboratory for Optoelectronics, Huazhong University of Science and Technology, China. He is currently pursuing a postdoctoral position at the City University of Hong Kong, China. His research interests are in the design and fabrication of near-infrared quantum dot optoelectronic devices, including characterization. Specific research efforts involve quantum dot/perovskite tandem photovoltaic devices and the preparation of various functional layers by vacuum- and solution-based methods.

Ruiheng Gao received his B.Eng. degree in Optoelectronic Information Science and Engineering from Sichuan University, China, in 2024. He is currently a master student in Optical Engineering at Huazhong University of Science and Technology, China, under the supervision of Prof.

Tianjun Ma obtained his bachelor's degree in Physics from Zhengzhou University, China, in 2021. Now he is a Ph.D. student at the Wuhan National Laboratory for Optoelectronics, Huazhong University of Science and Technology, China. Currently, his research interests focus on the high efficiency and excellent stability of all-perovskite tandem solar cells, especially those based on Pb-Sn mixed perovskite.

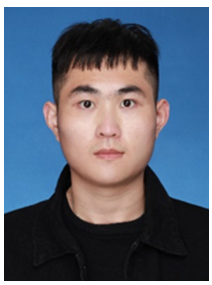

Yuheng Li is a Ph.D. Candidate at the Wuhan National Laboratory for Optoelectronics, Huazhong University of Science and Technology, China. His research focuses on high-performance single-junction and multi-junction inverted perovskite solar cells, emphasizing bandgap engineering, defect passivation, crystallization control, and interface engineering to enhance light absorption, reduce recombination losses, and improve efficiency and stability. He also studies conductive interconnection layers for tandem devices and uses aging tests and *in-situ* characterization to understand degradation and enable scalable photovoltaic applications.

Gomaa Mohamed Gomaa Khalaf is a postdoctoral Fellow at the School of Engineering Physics at Shenzhen Technology University (SZTU), China, since May 2025. At SZTU, Gomaa is focusing on PbS quantum dots for IR photovoltaics, aiming to address performance loss and degradation. He achieved a Ph.D. degree in Optical Engineering from Huazhong University of Science and Technology, China, with the title of "A Study of Quantum Dot Surface Ligand and Recombination Layer Toward All Quantum Dot Tandem Solar Cells". He has been permanently working as a researcher at the Solar Laboratory, Solar and Space Department, National Research Institute of Astronomy and Geophysics (NRIAG), Egypt. He has experience in QD research, including wide- and narrow-bandgap PbS QDs for solar cells, photodetectors, and imaging sensors.

Michael Wang finished college education in Shandong University, China, then received two M.E. degrees from University Toledo and Rutgers University, USA. From 2002 to 2007, he studied toward Ph.D. degree in a joint program between Rutgers University and Princeton University, USA. From 2001 to 2007, he worked for Hutchinson (Total) and received 2002 President's the 1st Award. From 2007 to 2013 he worked for Schlumberger as a Senior Mechanical Engineer and Senior Simulation & Modeling Engineer. From 2013 to 2022, he was the Principal Engineer with Sercel (CGG). From 2023 to present, he is a Lead Mechanical engineer with CNPC USA Corporation.

Chris Cheng received the B.E. degree in Mechanical Engineering from Tsinghua University, Beijing, China, in 1999, the Ph.D. degree in Industrial Engineering from The Ohio State University, Columbus, OH, USA, in 2005, and the Executive M.B.A. degree from the Jones Graduate School of Business, Rice University, Houston, TX, USA, in 2026.

In 2006, he joined Baker Hughes, Houston, TX, USA, as a Research Scientist, where he was engaged in research on numerical modeling, rock and fracture mechanics, downhole sensing, and Fitness-for-Service evaluation. In 2013, he joined CNPC USA, Houston, TX, USA, where he directed research and development of downhole drilling products and, since 2025, has served as Senior Director of Innovation and Technology. His current research interests include advanced drilling technology, materials science, and innovation strategy for upstream oil and gas applications. He has authored or coauthored numerous technical publications and holds more than 40 issued and published patents.

Dr. Cheng is a recipient of five industry awards and eight corporate excellence awards for his contributions to drilling technology and product innovation. He is a Member of the Society of Petroleum Engineers (SPE), the American Society of Mechanical Engineers (ASME), and the American Rock Mechanics Association (ARMA), and serves on the Gulf Energy Information Awards committee.

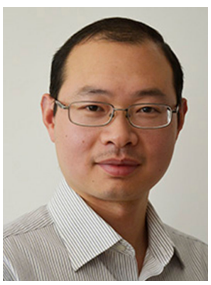

Jianbing Zhang is a professor and doctoral supervisor at Huazhong University of Science and Technology, China, specializing in quantum dot materials and optoelectronic devices. He earned his bachelor's, master's, and Ph.D. degrees in Electronic Science and Technology from the same university. During his research in the United States, he studied under Arthur J. Nozik, a leading authority in quantum dots and multi-exciton generation. His work on infrared quantum dots and optoelectronic applications has gained strong academic and industrial recognition. He has received the Hubei Natural Science Award (2019) and other major honors. His current research focuses on shortwave infrared imaging, spectral imaging, and high-definition microdisplays.

Ahmed Ghitas is a professor of solar energy physics and founder of the Photovoltaic Research and Applications Group at the National Research Institute of Astronomy and Geophysics (NRIAG), Egypt. He established the Photovoltaic Research Unit (PVU) at NRIAG and developed solar radiation and weather monitoring stations across the country. His research focuses on solar photovoltaics and renewable energy applications. Prof. Ghitas has published over 110 research articles and actively participated in more than 100 international and national conferences and workshops. He has supervised 9 M.Sc. and 7 Ph.D. students, led 8 funded research projects, and reviewed numerous projects, theses, and journal articles. He has held several leadership roles at NRIAG, including Vice President (2006–2025), Head of the Solar Research Laboratory, and Deputy Head of the Solar and Space Research Department. He currently serves as Director of PVU at NRIAG.

Haisheng Song is a professor and doctoral advisor at the Wuhan National Laboratory for Optoelectronics, Huazhong University of Science and Technology, China. He received his Bachelor's degree in Physics and Master's degree in Condensed Matter Physics from the School of Physical Science and Technology, Huazhong Normal University, China, in 2004 and 2007, respectively, and earned his Ph.D. degree from City University of Hong Kong, China, in 2010. From 2010 to 2012, he conducted postdoctoral research at the National Institute for Materials Science (NIMS) in Japan, and joined Huazhong University of Science and Technology in April 2012. He was promoted to Professor in 2018. His long-term research focuses on novel thin-film solar cells. As project leader, he has secured funding from various programs including the NSFC General Program, key projects under the National Key R&D Program, and basic research key projects supported by other ministerial-level institutions. He has published over 100 papers as corresponding author in renowned journals such as *Nature Photonics*, *Joule*, and *Nature Communications*, has been granted more than 10 invention patents, and has accumulated over 12,000 citations (Web of Science) with an H-index of 60.

Jiang Tang received his Bachelor's degree from the University of Science and Technology, China, in 2003, and Ph.D. degree in Materials Science and Engineering from the University of Toronto, Canada, in 2010. He spent 1.5 years as a postdoctoral researcher at the IBM T. J. Watson Research Center. Then he joined the Wuhan National Laboratory for Optoelectronics, Huazhong University of Science and Technology, China, as a professor in 2012. His group focuses on new-concept thin-film solar cells, halide perovskite nanocrystals for light-emitting applications, and single crystals for X-ray detection. He has published 400+ papers in prestigious magazines, including *Nature*, *Nature Materials*, *Nature Energy*, and *Nature Photonics*.